



Nickel dual-atom sites for electrochemical carbon dioxide reduction

Qi Hao^{1,2,7}, Hai-xia Zhong^{1,3,7}, Jia-zhi Wang^{1,4,7}, Kai-hua Liu^{1,7}, Jun-min Yan², Zhou-hong Ren⁵, Na Zhou^{1,4}, Xiao Zhao^{1b,2}, Hao Zhang⁶, Dong-xue Liu², Xi Liu^{1b,5}, Li-wei Chen⁵, Jun Luo⁶ and Xin-bo Zhang^{1,4}✉

Dual-atom catalysts, combining single-atom catalysts and metal alloys, are promising electrocatalysts for CO₂ reduction but are limited by sluggish CO₂ reduction kinetics and ill-defined dual-atom sites. Here, we develop a catalyst of Ni dual-atom sites via in situ conversion of nanoparticles into dual atoms. We achieve efficient electrocatalytic CO₂ reduction on Ni dual-atom catalysts with a CO partial current density up to $\sim 1\text{ A cm}^{-2}$ and turnover frequency of $77,500\text{ h}^{-1}$ at $>99\%$ Faradaic efficiency. In situ X-ray absorption and theoretical calculations reveal that during the catalytic process the Ni dual-atom sites trigger the adsorption of hydroxyl (OH_{ad}), forming electron-rich active centres that endow a moderate reaction kinetic barrier of *COOH formation and *CO desorption. The resultant catalytic microenvironment enables expedited kinetics compared with either the kinetics of bare dual-atom sites or OH_{ad} regulated single-atom sites.

Electrochemical CO₂ reduction reaction (CO₂RR) into value-added chemicals/fuels, coupled with renewable energy sources, is promising to address the environmental and energy crises and realize sustainable carbon neutrality^{1,2}. One important CO₂ valorization is electrochemical CO₂RR to CO, as CO is a key feedstock for the industrial Fischer–Tropsch process to produce valued products such as methane, methanol, diesel fuel, and so on³. Recently, considerable progress in electrocatalytic CO₂RR has been established with high CO selectivity ($\geq 90\%$) by suppressing the competitive hydrogen evolution reaction (HER). Unfortunately, the sluggish CO₂RR kinetics remain unsolved, even in widely acclaimed electrocatalytic systems, such as single-atom catalysts (SACs) consisting of isolated metal–nitrogen (N) sites^{4–6}. This arises from restricting the intrinsic scaling relationship of adsorption/desorption towards reactants/intermediates on single-atom sites⁷. It follows that their achieved current densities still fall far behind the commercial level ($\geq 250\text{ mA cm}^{-2}$)⁸. To this end, we sought to develop dual-atom catalysts (DACs) for high-efficiency and economical CO₂RR, as they bridge SACs and conventional bulk/nanoparticle/cluster catalysts (ensembles of atoms). Most strikingly, DACs can ideally overcome the limitation of single isolated sites via synergistically regulating the CO₂ activation and intermediate formation/desorption, thus allowing fast CO₂RR kinetics on their adjacent metal sites^{9–11}. However, limitations in the synthetic methods and lack of insightful fundamental studies on dual-atom sites hinder the development of DACs in high-efficiency CO₂RR^{12–14}.

Here, we report a carbon-rich DAC with Ni dual-atom sites (Ni₂NC) towards CO₂RR to CO, and investigate the catalytic behaviour of dual-atom sites. The atomic dispersion of Ni dual atoms was confirmed by aberration-corrected high-angle annular dark-field

scanning transmission electron microscopy (HAADF-STEM), together with X-ray absorption fine structure (XAFS) spectroscopy. The dynamic process of Ni species transformation was recorded by in situ environmental scanning transmission electron microscopy (ESTEM), indicating a combination of Ostwald ripening of forming the bulk phase and an atomization processes of converting bulk phase to dual-atom sites for synthesizing Ni DACs. In electrocatalytic CO₂ reduction to CO, Ni₂NC achieved an industrial-level performance, with a j_{CO} (current density towards CO product) up to 1 A cm^{-2} , a turnover frequency (TOF) of $77,500\text{ h}^{-1}$ at $\sim 99\%$ Faradaic efficiency (FE) and a half-reaction energy efficiency of 66%, as well as a 30 h stability at $\sim 290\text{ mA cm}^{-2}$. Ab initio molecular dynamics (AIMD) and free energy calculations, combined with in situ XAFS measurement, disclose that hydroxyl adsorbate (OH_{ad})-induced Ni dual-atom sites (Ni₂N₆OH) act as the real active sites towards fast CO₂RR kinetics and slower HER kinetics on Ni DAC. We also found that OH_{ad} can induce an electron-rich catalytic environment around Ni dual-atom sites and promote the CO₂RR process by the favourable CO₂ activation and reduced energy barrier for *COOH intermediate formation and *CO desorption. Our study indicates the crucial role of constructing dual-atom sites and optimizing their catalytic microenvironment for enhancing the catalytic activity of metal catalysts, and highlights that engineering DACs is compelling in boosting high-efficiency CO₂RR and other important complex catalytic reactions.

Results and discussion

Synthesis and characterization. Ni₂NC was prepared through the co-pyrolysis of Ni-citric acid complexes adsorbed on carbon carriers and dicyandiamide (DCD) at 800 °C. A Ni single-atom catalyst

¹State Key Laboratory of Rare Earth Resource Utilization, Changchun Institute of Applied Chemistry, Chinese Academy of Sciences, Changchun, P. R. China. ²Key Laboratory of Automobile Materials Ministry of Education and College of Materials Science and Engineering, Jilin University, Changchun, P. R. China. ³Center for Advancing Electronics Dresden (CFAED) and Faculty of Chemistry and Food Chemistry, Technische Universität Dresden, Dresden, Germany. ⁴University of Science and Technology of China, Hefei, P. R. China. ⁵School of Chemistry and Chemical Engineering, In-situ Center for Physical Sciences, Frontiers Science Center for Transformative Molecules, Shanghai Jiao Tong University, Shanghai, P. R. China. ⁶School of Materials Science and Engineering, Tianjin University of Technology, Tianjin, P. R. China. ⁷These authors contributed equally: Qi Hao, Hai-xia Zhong, Jia-zhi Wang, Kai-hua Liu. ✉e-mail: xbzhang@ciac.ac.cn

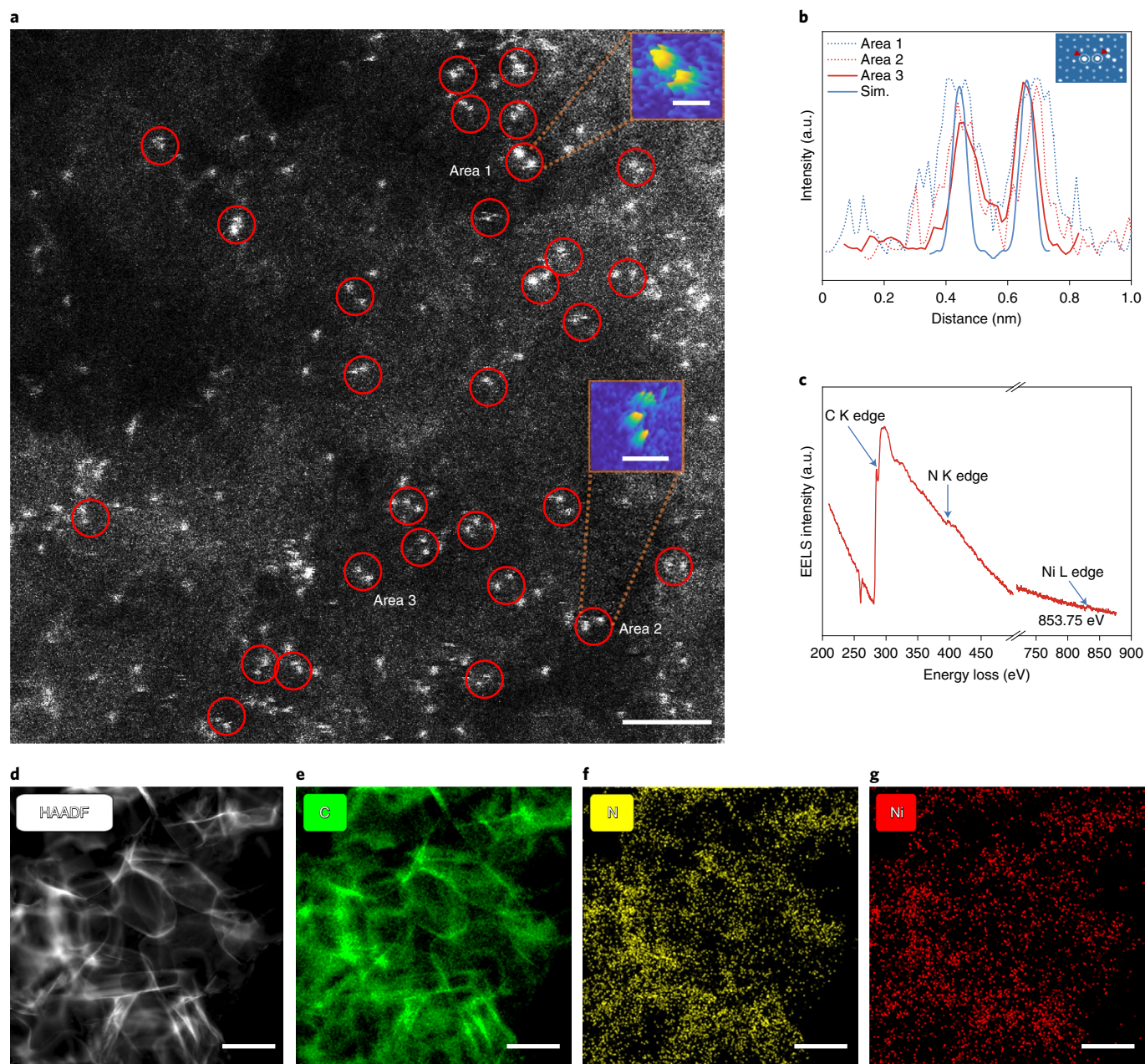


Fig. 1 | Morphology of Ni_2NC . **a**, HAADF-STEM image of Ni_2NC , the dimers are depicted in the red circles. Scale bar, 2 nm. Inset: the Ni–Ni atoms in the observed diatomic pair. Scale bar, 0.25 nm (area 1) and 0.5 nm (area 2). **b**, Atomic distance of dual atoms in the experimental and simulated (Sim.) STEM images. Inset: the theoretical model based on the simulated STEM image by quantitative STEM software. Scale bar, 0.25 nm; a.u., arbitrary units. **c**, EELS spectrum based on area 2 in **a**. **d–g**, HAADF-STEM of Ni_2NC (**d**) and corresponding elemental mapping images for C (**e**), N (**f**) and Ni (**g**). Scale bar, 200 nm.

(Ni_1NC) and Ni nanoparticles (Ni NPs) catalyst were also prepared as reference samples through a similar pyrolysis process. The scanning/transmission electron microscopy (SEM/TEM) and HAADF-STEM images (Supplementary Figs. 1–3) show that Ni_2NC and Ni_1NC inherit the intercross nanosheet morphology from NC, except for the extra wrinkles induced from the carbon corrosion by Ni species. Crystalline Ni species are excluded in Ni_2NC and Ni_1NC samples through TEM and X-ray diffraction analysis (Supplementary Fig. 4). In the HAADF-STEM images (Fig. 1a), numerous adjacent bright dots are observed for Ni_2NC . The observed average distance of these adjacent dots (~ 0.25 nm) approaches that of the adjacent Ni atoms (~ 0.24 nm) in the simulated STEM image depicted with the theoretical model (Fig. 1b and Supplementary Fig. 5), which

suggests that the two adjacent bright dots are assigned to Ni dual-atom sites¹⁵. Only isolated single bright dots are seen and recognized as Ni single-atom sites in Ni_1NC (Supplementary Fig. 6a,b)^{4,15}. The N K edge and Ni L edge (Fig. 1c and Supplementary Fig. 6c) in the electron energy loss spectra (EELS) further reveal the generation and stabilization of Ni dual/single atoms, which are anchored on NC by Ni–N bonds^{16–20}. The elemental mapping images (Fig. 1d–g and Supplementary Fig. 6d–g) verify a homogeneous distribution of Ni, N and C elements over Ni_2NC and Ni_1NC .

In situ ESTEM measurement was used to monitor the dynamic process of the transformation of Ni species during the pyrolysis process and investigate the formation mechanism of Ni dual atoms (Supplementary Figs. 7–9). As shown in Supplementary

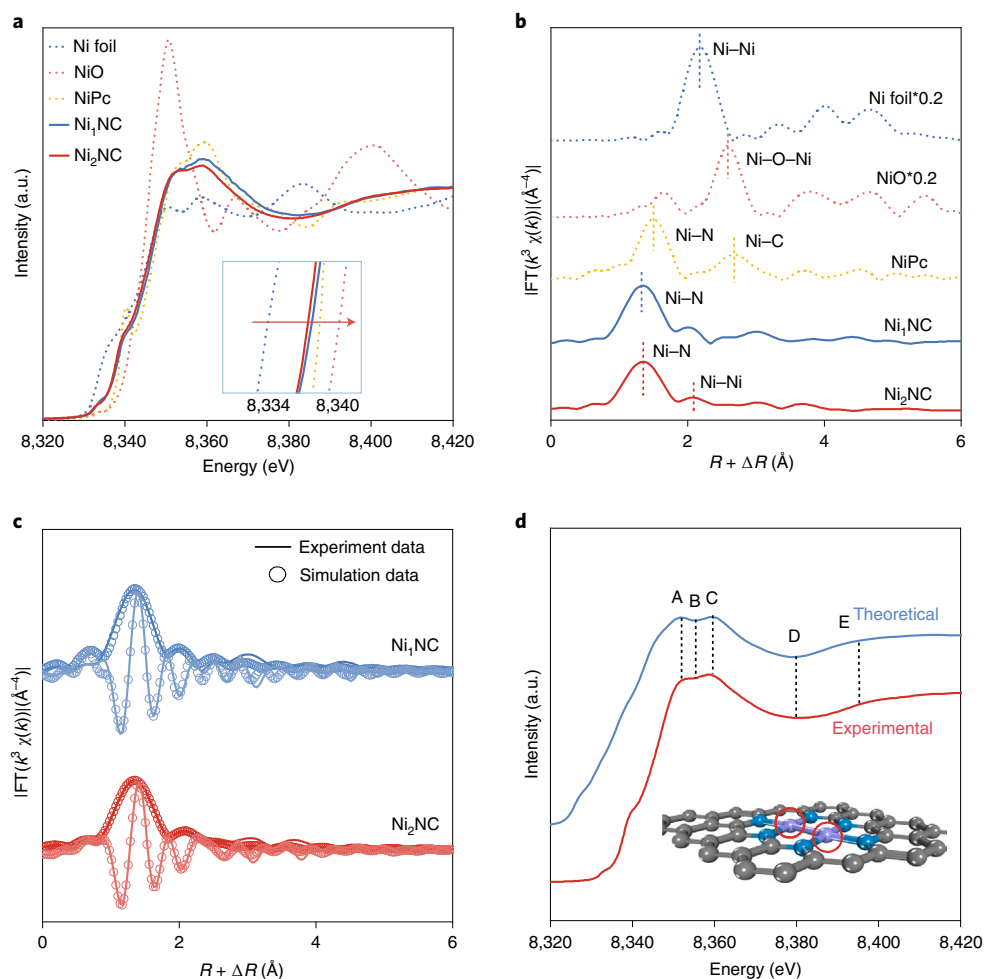


Fig. 2 | Structural characterizations of Ni_2NC and Ni_1NC . **a**, The XANES spectra at the Ni K edge of Ni foil, NiO, NiPc (nickel(II) phthalocyanine), Ni_1NC and Ni_2NC . **b**, Fourier transforms (FT) of k^3 -weighted Ni K edge EXAFS experimental data for Ni foil, NiO, NiPc, Ni_1NC and Ni_2NC . **c**, Fourier transforms of k^3 -weighted Ni K edge EXAFS experimental data and fitted data of the real parts and imaginary parts for Ni_1NC and Ni_2NC . **d**, A comparison between the experimental XANES spectrum and the theoretical spectrum for Ni_2NC . The main features reproduced are highlighted at points A–E. The grey, turquoise and purple spheres represent carbon, nitrogen and nickel atoms, respectively. The Ni atoms with red circles mean the adsorbing atoms in the XANES spectrum.

Figs. 7 and 8, Ni complexes on carbon carriers were first transformed into nanoparticles at 200 °C. Next, the crystalline Ni NPs grew larger through an Ostwald ripening process until 500 °C. When the temperature was raised to 700 °C, bulk-phase Ni species began to dissolve, and eventually disappeared at 800 °C. Next, we adopted Ni_{10} as an example to investigate the formation mechanism (Supplementary Fig. 10) by theoretical calculation. The formation of the first Ni atom in the N_6 defect from the decomposition of the Ni_{10} cluster requires a kinetic barrier of 1.16 eV. A barrier of 1.47 eV must be overcome to subsequently form the second Ni atom in the N_6 defect from the decomposition of the Ni_9 cluster. However, the formation of Ni single atom in the N_4 defect requires a higher barrier of 2.08 eV. Therefore, the formation of Ni dual-atom sites was dominant at high temperatures. Thus, we deduce that the evaporated Ni atoms were captured by the double carbon vacancies in the carbon carrier during the pyrolysis process and thus form dual-atom sites (Supplementary Fig. 11), which is different from the typical atomization process for synthesis of Ni single atoms¹⁶. In addition, it is worth noting that the pyrolysis temperature, amount of nitrogen source (ammonia additives) and molar ratios of metal precursors and chelating agents will affect the generation/dispersion and

chemical structure of Ni atoms, and corresponding Ni loading (see details in Supplementary Figs. 12–25 and Tables 1–3).

The chemical structures of Ni_2NC and Ni_1NC were investigated using the XAFS technique. The pre-edge of Ni_2NC (~8,338 eV) and Ni_1NC (8,339 eV) between those of Ni foil and NiPc (Fig. 2a) reveal the valence of Ni as being between 0 and +2 (refs. 18,19). The lower binding energy of the Ni $2p_{3/2}$ peak for Ni_2NC (855.3 eV) than for Ni_1NC (855.7 eV) verifies the lower Ni oxidation state in Ni_2NC samples (Supplementary Fig. 26)^{7,9}. In addition, the fitted Ni–N peak in the high-resolution N 1s X-ray photoelectron spectroscopy (XPS) spectra of Ni_2NC and Ni_1NC (Supplementary Fig. 27) indicates the Ni–N coordination in Ni_2NC and Ni_1NC .

The extended X-ray absorption fine structure (EXAFS) technique was further employed to analyse the coordination environment of Ni. The prominent peak for the Ni–N shell was found at ~1.45 and 1.44 Å for Ni_2NC and Ni_1NC , respectively (Fig. 2b)¹⁷. Meanwhile, the Ni–Ni peak is only observed for Ni_2NC (2.09 Å), which is highly relevant to the feature of Ni dual atoms for Ni_2NC and isolated single Ni atoms for Ni_1NC , respectively. The fitted coordination numbers (CNs) of N and Ni were, separately, 3.1 and 0.9, with the bond lengths of 1.89 Å (Ni–N) and 2.51 Å (Ni–Ni) for

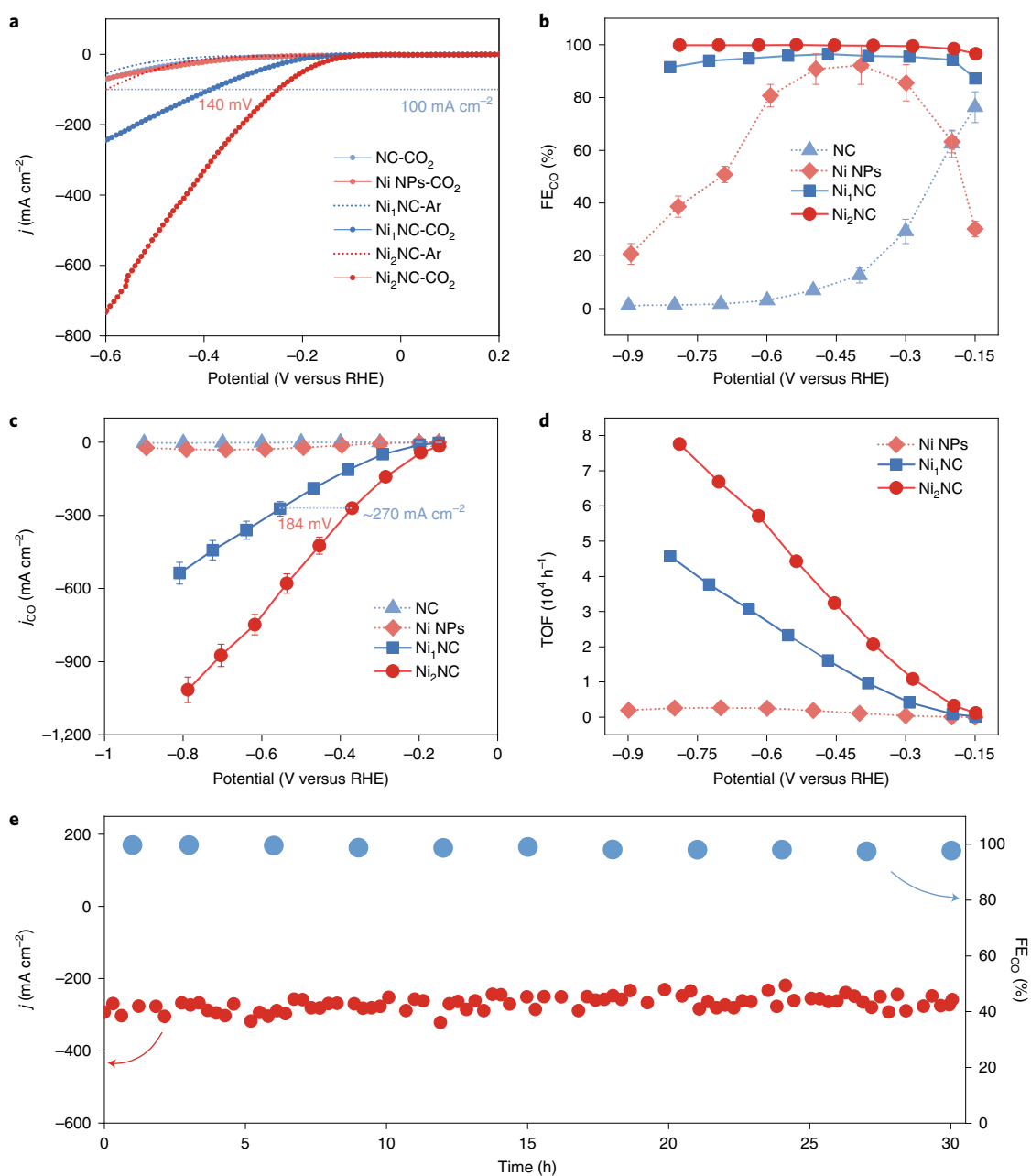


Fig. 3 | Electrocatalytic CO₂ activity using flow cell with 1M KOH electrolyte. **a**, Linear sweep voltammograms of Ni₂NC, Ni₁NC, Ni NPs and NC under CO₂ and Ar atmospheres. **b**, FE of CO for Ni₂NC, Ni₁NC, Ni NPs and NC. **c**, Specific CO partial current density (j_{CO}) of Ni₂NC, Ni₁NC, Ni NPs and NC. **d**, TOFs of Ni₂NC, Ni₁NC and Ni NPs. **e**, Long-term stability of Ni₂NC in electrocatalytic CO₂ at -0.37 V versus RHE.

Ni₂NC. The CN of N for Ni₁NC was 3.7, with a Ni–N bond length of 1.86 Å (Supplementary Table 4). On the basis of the experimental and fitted Fourier transform-EXAFS spectra at R space (Fig. 2c), the local structure is proposed as N₃–Ni–Ni–N₃ (Ni₂N₆) for Ni₂NC and NiN₄ for Ni₁NC. Accordingly, the simulated X-ray adsorption near-edge structure (XANES) spectrum of Ni₂NC (Fig. 2d) is consistent with the experimental spectrum, further elucidating that the coordination structure of the main Ni species is Ni₂N₆. The minor differences between the experimental and theoretical XANES spectra originate from the inevitable existence of single-atom and cluster species. Two intensity maximums at $\sim 6 \text{ \AA}^{-1}$ and $\sim 8 \text{ \AA}^{-1}$ (Supplementary Fig. 28g) are observed in the EXAFS wavelet transform spectrum of Ni₂NC, and are assigned to Ni–N and Ni–Ni bonding, respectively. Only the Ni–N shell signal (6 \AA^{-1}) is

detected for Ni₁NC (Supplementary Fig. 28f)¹¹. The comparisons of the q -space magnitudes for FEFF-calculated k^2 -weighted EXAFS paths (Supplementary Fig. 28d) further confirm the Ni–Ni path (6.50 \AA^{-1}) and Ni–N path (8.70 \AA^{-1}) for Ni₂NC, with only the Ni–N path (6.40 \AA^{-1}) for Ni₁NC. These results synergistically clarify the atomic dispersion of Ni dual-atom sites in Ni₂NC.

Temperature-programmed desorption analysis detects dominant chemisorption of CO₂ molecule (~ 350 – 450°C) for Ni₂NC, which contributes to its high CO₂ adsorption capacity at room temperature ($22 \text{ cm}^3 \text{ g}^{-1}$; Supplementary Fig. 29). Interestingly, superhydrophobicity is observed on Ni₂NC with a contact angle of 151° (Supplementary Fig. 30), which will facilitate the three-phase interfacial reaction, suppress the electrode flooding and accelerate gas transfer during the catalytic process^{21,22}.

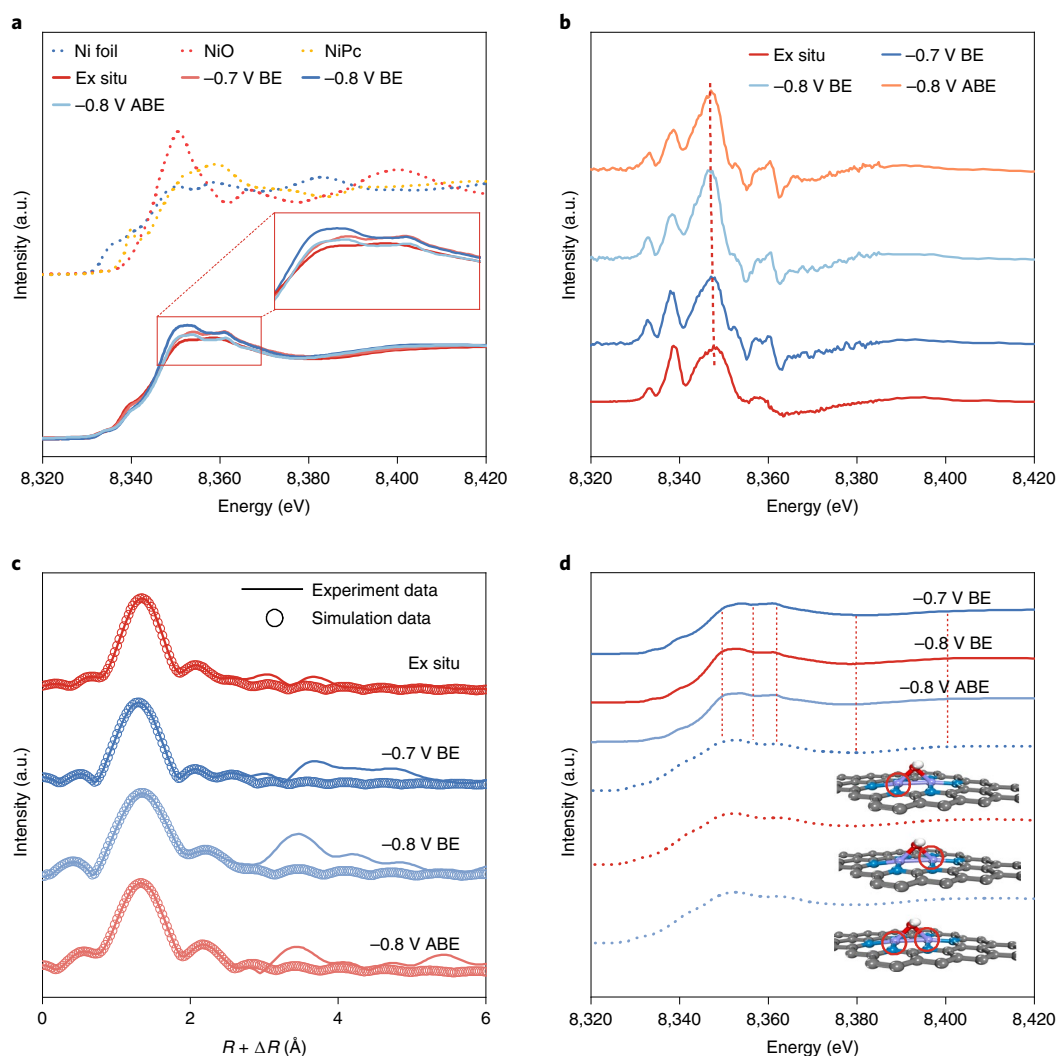


Fig. 4 | In situ XAFS analysis. **a**, The XANES spectra recorded at Ni K edge of Ni₂NC at different applied potentials; BE and ABE represent bulk electrolysis and after bulk electrolysis, respectively. **b**, The first derivative of XANES, the vertical dotted line indicates the tendency of the valence state shift. **c**, The Fourier transforms of k^3 -weighted Ni K edge EXAFS experimental data and fitted data for Ni₂NC. **d**, Comparing the experimental XANES spectra (solid lines) and the theoretical spectra (dotted lines) calculated with the depicted structures. The main features reproduced are highlighted by the vertical dotted lines. The atoms with red circles represent the adsorbing atoms in XANES spectra, the grey, turquoise, red, white and purple spheres represent carbon, nitrogen, oxygen, hydrogen and nickel atoms, respectively.

CO₂RR activity evaluation. Electrocatalytic CO₂RR on all samples was first assessed in an H-type cell (Supplementary Fig. 31). Only gas products (CO and H₂) are detected in our catalytic systems (Supplementary Figs. 31 and 32). Ni₂NC exhibits an excellent selectivity in electrocatalytic CO₂-to-CO. Its FE_{CO} reaches 98.7% from -0.4 to -0.9 V versus RHE (reversible hydrogen electrode), outperforming that of Ni₁NC (90%), Ni NPs (80%) and NC (20%). The feasibility of Ni₂NC in practical electrocatalytic CO₂RR was further evaluated in a flow cell with 1 M KOH electrolyte, as alkaline electrolyte can effectively inhibit HER, promote the activation of CO₂ molecules and lower the kinetic barriers of intermediate formation and desorption (Supplementary Fig. 33)²³. In 1 M KOH electrolyte, Ni₂NC exhibits the lowest onset potential among the catalysts (Fig. 3a). The FE_{CO} of Ni₂NC is maintained at ~99% over the applied potentials (Fig. 3b), while it is ~96% for Ni₁NC. Importantly, Ni₂NC achieves a breakthrough j_{CO} up to ~1 A cm⁻² at an FE_{CO} of 99%, which is double the value of Ni₁NC (~0.53 A cm⁻²) (Fig. 3c), far surpassing the recorded values for CO₂RR to CO (Supplementary Table 5) and highlighting the significant role of synergistically

utilizing adjacent Ni atoms in accelerating CO₂RR. Negligible j_{CO} (<0.03 A cm⁻²) with the lower FE_{CO} of NC and Ni NPs than Ni₁NC and Ni₂NC underlines the advantage of atomically dispersed Ni-N sites in electrocatalytic CO₂RR. The excellent catalytic activity of Ni₂NC is also gleaned from its larger TOF of 77,500 h⁻¹ compared with Ni₁NC (45,680 h⁻¹) and Ni NPs (1,940 h⁻¹) (Fig. 3d), suggesting that dual-atom sites possess a superior intrinsic activity and a faster reaction rate for electrocatalytic CO₂RR compared to single-atom or particle sites. Importantly, the Ni₂NC demonstrates an energy-efficient CO₂RR process with a superior half-reaction energy efficiency (~66% at j_{CO} of 1 A cm⁻²) (Supplementary Fig. 34). Moreover, Ni₂NC achieves lower overpotential (15.33 mA cm⁻², 38 mV) and larger j_{CO} (579.3 mA cm⁻², 430 mV) in 1 M KOH than those obtained in 1 M KHCO₃ (16.73 mA cm⁻², 280 mV; 375.1 mA cm⁻², 464 mV) (Fig. 3 and Supplementary Fig. 35), manifesting the faster reaction kinetics in the alkaline system. The lower Tafel slope (69.6 mV dec⁻¹) obtained by Ni₂NC compared with Ni₁NC (131 mV dec⁻¹), Ni NPs (252 mV dec⁻¹) and NC (170 mV dec⁻¹) further suggests its faster CO₂RR kinetics (Supplementary Fig. 31c)^{24,25}. Ni₂NC also

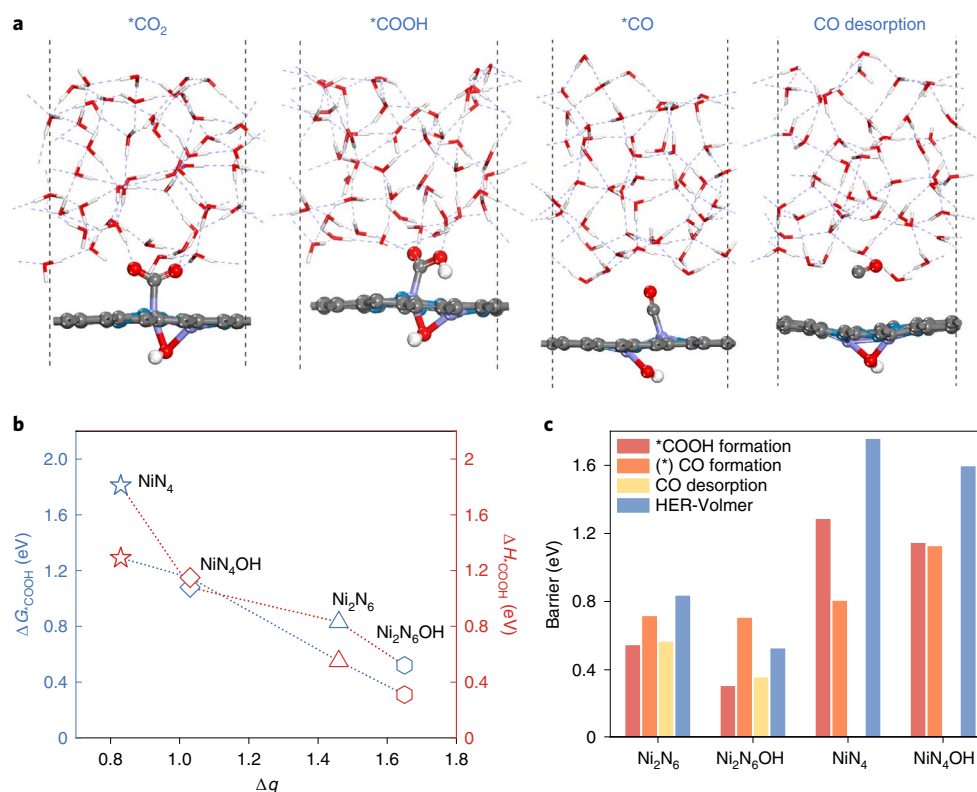


Fig. 5 | DFT calculations. **a**, Reaction pathways for the $^*\text{COOH}$ formation, $^*\text{CO}$ formation and $^*\text{CO}$ desorption on $\text{Ni}_2\text{N}_6\text{OH}$. The grey, turquoise, red, white and purple spheres represent carbon, nitrogen, oxygen, hydrogen and nickel atoms, respectively. **b**, The relationship between Bader charges (Δq) and Gibbs free energy/Helmholtz free energy for $^*\text{COOH}$ formation on different sites. **c**, Kinetic barriers for different adsorbates on Ni_2N_6 , $\text{Ni}_2\text{N}_6\text{OH}$, NiN_4 and NiN_4OH sites.

shows lower charge transfer resistance during the CO_2RR process than Ni_1NC in electrochemical impedance spectroscopy (EIS) (Supplementary Fig. 36a and Supplementary Table 6). In addition, the larger electrochemical active surface area of Ni_2NC was reflected by its higher electrochemical double-layer capacitance (C_{dl} , 31.31 mF cm^{-2} ; Supplementary Fig. 36b) than that of Ni_1NC (14.5 mF cm^{-2}), Ni NPs (7.38 mF cm^{-2}) and NC (7.31 mF cm^{-2}). This is associated with its higher Brunauer–Emmett–Teller surface area ($270.8 \text{ m}^2 \text{ g}^{-1}$; Supplementary Table 7) than for Ni_1NC ($239.1 \text{ m}^2 \text{ g}^{-1}$), Ni NPs ($201.2 \text{ m}^2 \text{ g}^{-1}$) and NC ($209.3 \text{ m}^2 \text{ g}^{-1}$), and abundant pores and defects (Supplementary Figs. 37 and 38)^{7,26}. These features endow Ni_2NC with more electrochemical active Ni sites ($19.20 \text{ nmol cm}^{-2}$; Supplementary Fig. 39) than Ni_1NC ($4.81 \text{ nmol cm}^{-2}$) despite their similar Ni loadings (0.29 at% for Ni_2NC ; 0.26 at% for Ni_1NC) indicated by inductively coupled plasma optical emission spectrometry detection (Supplementary Table 1).

Importantly, Ni_2NC achieved a remarkable long-term durability in a flow cell with no apparent degradation of current density ($\sim 290 \text{ mA cm}^{-2}$) under 30 h operation (Fig. 3e). The slight decay of FE_{CO} to 97% probably stems from the flooding issue and carbonate accumulation on the electrode rather than disabling of the Ni_2NC catalyst. In an H-type cell, Ni_2NC is robust over 100 h electrolysis (Supplementary Fig. 31d). HAADF-STEM, ex situ X-ray diffraction and XPS analysis disclose that the preservation of the atomically dispersed Ni dual atoms free of Ni particles is responsible for the long-term durability of Ni_2NC (Supplementary Figs. 40 and 41). Thereby, Ni_2NC with exceptional activity and robust stability is of great value in electrocatalytic CO_2RR .

The electrocatalytic activities of the contrast Ni_2NC samples were also investigated (Supplementary Fig. 42). The j_{CO} and FE_{CO} for $\text{Ni}_2\text{NC-700}$ (311.1 mA cm^{-2} ; 90.2%), $\text{Ni}_2\text{NC-900}$

(561.5 mA cm^{-2} ; 98.1%), $\text{Ni}_2\text{NC-0.5}$ (439.7 mA cm^{-2} ; 93.3%), $\text{Ni}_2\text{NC-1.5}$ (464.1 mA cm^{-2} ; 94.9%), $\text{Ni}_2\text{NC-1/2}$ (403.4 mA cm^{-2} ; 98.0%) and $\text{Ni}_2\text{NC-1/4}$ (657.6 mA cm^{-2} ; 98.7%) are all lower than the target Ni_2NC samples ($1,000 \text{ mA cm}^{-2}$; $\sim 99\%$; Supplementary Table 8). These results highlight the superiority of Ni dual atoms in promoting CO_2RR over Ni clusters and the important contribution of Ni loading to increasing j_{CO} of Ni_2NC samples. Therefore, synergistically controlling the generation/dispersion and structure of Ni dual atoms and Ni loading for Ni_2NC samples, by optimizing the pyrolysis temperature, amounts of nitrogen source and the molar ratio of metal precursors and chelating agents, will greatly affect their CO_2RR behaviours.

In situ attenuated total reflection-infrared (ATR-IR) spectroscopy measurement was undertaken to identify the occurrence of CO_2 reduction to CO on Ni_2NC . Over the applied potentials, the C–O stretching and OH deformation bands of the $^*\text{COOH}$ intermediate separately emerge at $1,353.3 \text{ cm}^{-1}$ and $1,278.6 \text{ cm}^{-1}$ for Ni_2NC . The gradually rising band at $1,918.8 \text{ cm}^{-1}$ under operational potentials lower than -0.8 V versus RHE was ascribed to $^*\text{CO}$ (Supplementary Fig. 43)^{27,28}.

Unveiling the active sites. In situ XAFS was applied to investigate the Ni dual-atom sites of Ni_2NC during the catalytic process in the flow cell system. As shown in the XANES spectra (Fig. 4a), the pre-edge of Ni_2NC samples during the CO_2RR process is still located between that for Ni foil and NiO, excluding the formation of metallic Ni¹⁰. The first derivative of XANES in Fig. 4b suggests a slight decrease in the oxidation state of Ni during the CO_2RR process due to charge transfer from the active sites to reactants and intermediates⁴. All Ni_2NC samples show a distinct Ni–N scattering path peak at $\sim 1.34 \text{ \AA}$, with no apparent changes in the Fourier

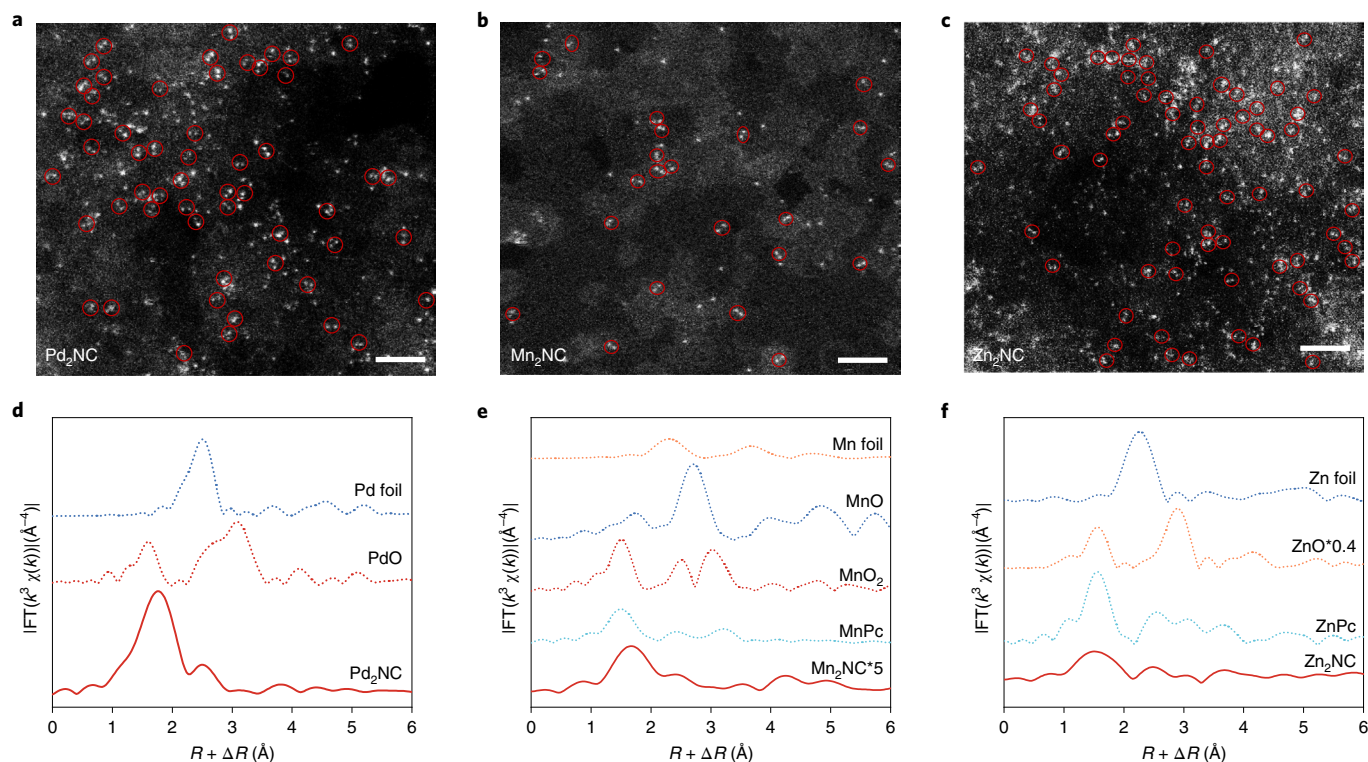


Fig. 6 | Characterizations of other M_2NC catalysts. **a–c**, HAADF-STEM images of Pd_2NC (**a**), Mn_2NC (**b**) and Zn_2NC (**c**). Scale bars, 2 nm. **d–f**, Fourier transforms of k^3 -weighted Pd, Mn or Zn K edge EXAFS experimental data for Pd_2NC (**d**), Mn_2NC (**e**) and Zn_2NC (**f**).

transform-EXAFS spectra (Fig. 4c) under the CO_2RR turnover conditions, further suggesting the excellent stability of Ni_2NC . Slight variation in the CN ($\Delta N \leq 0.1$) and bond distance ($R, \Delta R \leq 0.05$) of the Ni–N and Ni–Ni shell are found on Ni_2NC under electrolysis conditions (Supplementary Table 9). This is due to the changed electronegativity of Ni induced by the absorption of reactants or intermediates ($*CO_2$, $*COOH$, $*CO$, $*OH$, and so on)²⁹, which is also verified by the in situ ATR-IR analysis. Different from the Ni_2NC powder sample, the experimental XANES spectra of Ni_2NC during the CO_2RR process agree well with the theoretical XANES spectra depicted with the theoretical models (Ni_2N_6OH) (Fig. 4d). These results indicate that the Ni dual-atom sites will spontaneously adsorb hydroxide ions on applying the potential, in turn, which thus alters the microenvironment around the Ni active sites^{30,31}.

Catalytic mechanism. To illustrate the real electrocatalytic CO_2RR process of Ni_2NC , ab initio molecular dynamics were applied to investigate the kinetics of CO_2RR in a water environment (Fig. 5 and Supplementary Figs. 44–50)^{32,33}. Unlike the free energy calculations under a vacuum environment, the kinetics calculations proceed without fixing the CO_2 adsorption at a particular position. The structural evolution of the Ni_2N_6OH site occurred during the electrochemical steps (Fig. 5a). This shows the stable position of the adsorption configuration while the position of OH_{ad} changed during the catalytic process, which will bring the regulated catalytic sites towards a reduced overall reaction energy barrier. To further understand the modulation effect of OH_{ad} on the catalytic sites, a model of NiN_4OH was also considered. The kinetic barriers for different steps on various active sites and the relationship between the charge capacity of the central Ni sites and the formation energy of the $*COOH$ intermediate are shown separately in Fig. 5b,c. The results suggest that the OH_{ad} -induced increases in the charges of the central Ni sites will facilitate the CO_2 activation and lead to lower formation energies of $*COOH$ on OH_{ad} Ni sites compared to those on

OH_{ad} -free Ni sites. The relationship of Δq (Bader charges; Supplementary Table 10) and $\Delta G_{COOH}/\Delta H_{COOH}$ further reveals that the introduction of OH_{ad} increases the charge of the active sites and induces an electron-rich catalytic microenvironment, which will strengthen the adsorption of the key intermediate of $*COOH$ and deliver an optimized CO_2 reduction process (Fig. 5b). Indeed, the CO_2RR thermodynamics are promoted on the OH_{ad} -induced Ni atom sites (Ni_2N_6OH and NiN_4OH) for Ni SACs and DACs, as verified by the calculated vacuum Gibbs free energy for these electrochemical steps (Supplementary Fig. 51). When the Ni_2N_6 site is regulated by OH_{ad} , the energy barrier for $*COOH$ formation on Ni DACs with the resultant Ni_2N_6OH sites is decreased to 0.31 eV. In addition, the barrier for $*CO$ desorption on the Ni_2N_6OH site (0.36 eV) is also lower than that of the Ni_2N_6 site (0.56 eV) despite their similar barrier for the $*CO$ formation step (0.71 eV). The NiN_4OH site also shows a reduced energy barrier for $*COOH$ formation (1.08 eV) compared to its counterpart NiN_4 site (1.26 eV). Figure 5c also discloses the faster reaction kinetics on dual-atom sites than on single-atom sites, due to the lower barriers for the electrochemical steps of forming $*COOH$ on Ni_2N_6 sites (0.55 eV) compared to NiN_4 sites (1.26 eV) (Supplementary Figs. 52–57). Thus, the rapid CO_2RR kinetics for Ni DACs originate from that the adsorbed hydroxyl (OH_{ad})-induced Ni dual-atom catalytic sites (Ni_2N_6OH) effectively facilitating $*COOH$ formation and $*CO$ desorption³⁴. The calculated kinetic barriers of the HER-Volmer step on Ni single- and dual-atom sites also suggest that CO_2RR possesses faster kinetics than the competing HER, accounting for their high selectivity for CO_2 -to- CO (Fig. 5c).

Synthesis of other dual-atom catalysts. Notably, other M_2NC ($M = Zn, Mn$ and Pd) were successfully fabricated via this ligand-mediated method by merely replacing nickel(II) acetate tetrahydrate with zinc acetate dihydrate, manganese acetate and palladium chloride, respectively (Fig. 6, Supplementary Figs. 58–67 and

Supplementary Table 11). The metal K edge experimental XANES and XPS spectra of the as-prepared M_2NC disclosed the valence of M as between 0 and +2. The M–N and M–M bonds were identified by the EXAFS analysis. The good correlation between their theoretical and experimental XANES spectra (Supplementary Figs. 68–72) further suggested that the main coordination structure of the metal species in these DACs is M_2N_6 (ref. ³¹). The atomic dispersion of M_2 atoms on the NC substrate is confirmed for M_2NC through HAADF-STEM imaging^{35,36}. No aggregated bulk metallic particles were detected in these TEM images and X-ray diffraction patterns (Supplementary Figs. 58, 61, 64 and 67). These results demonstrate that the preparation of M_2NC follows the same procedure as Ni_2NC . Moreover, the controllable synthesis of DACs on a gram-level scale (up to 2 g) is realized via this strategy as well, which is beneficial for the application of DACs in practical catalysis (Supplementary Fig. 73).

Discussion. In summary, we developed well-defined and uniform Ni DACs and achieved an industrial-level CO_2RR performance with high activity and robust stability. The in situ ESTEM and transition-state calculations reveal the formation mechanism of the dual-atom sites. This universal synthetic method can be expanded to develop other dual-atom catalysts (for example, Pd_2NC , Mn_2NC and Zn_2NC). According to theoretical calculations and in situ XAFS techniques, Ni dual-atom sites allow a significantly boosted electrochemical CO_2 reduction through sufficient CO_2 activation and appropriate adsorption/desorption of the key intermediates via an OH_{ad} -optimized catalytic microenvironment around Ni dual-atom sites (Ni_2N_6OH). Taken together these endow Ni_2NC with superior reaction kinetics and selectivity towards CO production. This work paves the way for a universal method to fabricate DACs in pursuit of exceptional electrocatalytic activity, speeds up the development of effective electrocatalysts for industrial electrolytic CO_2RR and encourages the rational design/application of new DACs in other critical catalytic reactions.

Methods

Chemicals and materials. Nickel(II) acetate tetrahydrate (Aladdin, N112914, $NiC_4H_6O_4 \cdot 4H_2O$, 99%), manganese acetate (Aladdin, M110793, $MnC_4H_6O_4 \cdot 4H_2O$, AR), zinc acetate dihydrate (Aladdin, Z110777, $C_6H_8O_7 \cdot Zn \cdot 2H_2O$, AR), palladium chloride (Aladdin, P196359, $PdCl_2$, 99.999%, metal basis), ammonia solution (Aladdin, A112077, $NH_3 \cdot H_2O$, 25–28%, AR), citric acid monohydrate (Aladdin, C112632, $C_6H_8O_7 \cdot H_2O$, AR), dicyandiamide (Aladdin, D100429, $C_2H_4N_4$, 98%), potassium bicarbonate (Aladdin, P110485, $KHCO_3$, 99.5%), hydrochloric acid solution (Beijing Chemical Works, A0300003, HCl, 35–38%), sodium citrate tribasic dihydrate (S116311, $C_6H_5Na_3O_7 \cdot 2H_2O$, 99%), ethanol (Beijing Chemical Works, C₂H₅OH, B0301002, $\geq 99.8\%$), sulfuric acid (H_2SO_4 , Aldrich, 98%), 5% Nafion solution (Dupont), 212 Nafion membrane (Alfa Aesar), anion-exchange membrane (Fumasep, FAA-PK-130), ultrapure water (Millipore, 18.2 M Ω cm) used for all processes, Ar and CO_2 (Changchun Juyang Gas Ltd, $\geq 99.999\%$), carbon paper (CeTech, N1S1007), gas diffusion electrode (Sigracet, 39BB). These chemicals were used without further purification.

Preparation of carbon substrate. Sodium citrate tribasic dihydrate (10 g) was dried in an oven at a temperature of 150 °C for 48 h. Then, the reaction temperature was decreased to room temperature, and a white powder was obtained and transferred into a porcelain boat and heated for 1 hour at a fixed temperature (800 °C) and a temperature ramp rate of 5 °C min⁻¹ using Ar flow. The harvested black powder was treated with 5 M H_2SO_4 solution for 12 h at 80 °C, and several washing processes with ultrapure water and ethanol, as well as 6 h drying at 75 °C.

Preparation of NC. As-synthesized carbon substrate (100 mg) and dicyandiamide (1 g) were well mixed by grinding together and heated for 2 hours at 800 °C (temperature rate of 5 °C min⁻¹) using gas flow of Ar. Then, NC was collected through a washing process using ultrapure water and ethanol and a 6 h drying process at a fixed temperature of 75 °C.

Preparation of Ni_2NC and Ni_1NC . First, nickel(II) acetate tetrahydrate (12.8 mg) and citric acid monohydrate (32.2 mg) were dissolved in 2 ml of ethanol and the solution kept at room temperature with stirring for 1 h. Subsequently, on adding the carbon substrate (100 mg) into the solution, the mixture was stirred continuously under ambient conditions for 6 h, and the resulting dispersion

changed to a black solid after 12 h drying at 75 °C. After grinding with dicyandiamide (1 g) in a mortar, the black solid was transferred into a porcelain boat. The black solid was heated for 2 h at 800 °C with a temperature rate of 5 °C min⁻¹ with an Ar stream. Ni_2NC was obtained after washing several times with 3 M HCl solution and ultrapure water, and then drying for 12 h at 80 °C. Ni_1NC was obtained using a similar procedure, except that ammonia solution (50 μ l) was added in the first step. To study the influence of pyrolysis temperature, the molar ratio of metal precursors and chelating agent (citric acid) and the amount of nitrogen source (dicyandiamide) on the morphology and the dispersion of dual metal atom on NC, more contrast samples were synthesized as follows: (1) the pyrolysis temperature was varied from 800 °C to 700 °C and 900 °C; (2) the ratio of metal precursors and chelating agents was changed from 1:3 to 1:2 and 1:4; and (3) the amount of dicyandiamide was changed from 1 g to 0.5 g and 1.5 g. Additionally, large-scale synthesis of Ni_2NC was carried out with 20-fold higher amounts of precursors compared to the above synthesis procedure for Ni_2NC .

Preparation of Mn_2NC , Zn_2NC and Pd_2NC . Mn_2NC , Zn_2NC and Pd_2NC were synthesized using a similar procedure to that used for fabricating Ni_2NC . The amounts of the metal salt and citric acid monohydrate used in each synthesis were: manganese acetate (4.5 mg) and citric acid monohydrate (11.48 mg); zinc acetate dihydrate (3.4 mg) and citric acid monohydrate (9.64 mg); palladium chloride (1.67 mg) and citric acid monohydrate (5.92 mg).

Characterization. An X-ray diffractometer (micro-XRD, Rigaku, Japan) with Cu K α radiation with $\lambda = 0.15406$ nm was used to collect the powder X-ray diffraction patterns. The SEM images were undertaken using an Hitachi S4800 field emission scanning electron microscope, with an accelerating voltage fixed at 10 kV. TEM was performed on a JEM-2100F instrument, wherein the field emission gun operating voltage was set at 200 kV. An FEI Titan Themis 60-300 instrument was adapted to collect the HAADF-STEM analysis and relevant element mapping with energy-dispersive spectroscopy, with the working voltage of the spherical aberration corrector set at 200 kV. A micro-Raman spectrometer (Renwashaw) was used to obtain the Raman spectra. The Fourier transform infrared (FTIR) spectra were acquired using a Nicolet 6700 FTIR spectrometer. N_2 adsorption/desorption isotherms were recorded using a Micromeritics ASAP 2020. The CO_2 temperature-programmed desorption profiles were obtained using a Micromeritics Autochem chemical adsorption instrument. A ThermoFisher Scientific ESCALAB 250Xi spectrometer was used to record the XPS spectra, with the spectra calibrated on the basis of the C 1s binding energy at 284.4 eV. Electrochemical measurements were undertaken using a Biologic VMP3 electrochemical workstation under ambient conditions. NMR spectra were collected using a Bruker NMR spectrometer (AVANCE-III HD 500). Gas components analysis was performed on a ThermoFisher Trace 1300 gas chromatograph with pulsed discharge and flame ionization detectors. The Ni loading of catalysts was measured on an inductively coupled plasma optical emission spectroscopy (PE Avio 200).

Electrode preparation. Catalyst (5 mg) was dispersed in the mixed solvent of ethanol (950 μ l) and Nafion solution (50 μ l, 5 wt% in ethanol). After sonication for 1 h, the homogeneous catalyst suspension was drop-casted onto carbon paper and the gas diffusion layer (reaction area of H-type cell, 1 cm²; reaction area of flow cell, 1.1 cm²). The catalyst loading on the electrode was 0.5 mg cm⁻² in the H-type cell and 1.0 mg cm⁻² in the flow cell, respectively. Notably, the geometric surface area of the electrode was adapted to calculate the current density.

Electrochemical measurements. A Biologic VMP3 electrochemical workstation was used for all electrochemical measurements under ambient conditions. The CO_2 electrochemical reduction was tested in a traditional H-type cell with Nafion 212 film separating the components and a homemade flow cell (separated by FAA-PK-130) system (Supplementary Fig. 35). Pt mesh and Ni foam were used as the counter electrode for H-type and flow cell systems, respectively. The reference electrode was an Ag/AgCl electrode. All applied potentials were changed to those with respect to the RHE on the basis of the equation, $E_{RHE} = E_{Ag/AgCl} + 0.05916 \times pH + 0.197 + E_{iR}$, and the scan rate of the linear sweep and cyclic voltammetry curves was 10 mV s⁻¹. An a.c. voltage with a voltage amplitude of 10 mV was applied during the EIS testing process over a varying frequency (100 kHz–0.1 Hz). The electrochemical active surface area was evaluated by C_{dl} , which was acquired from cyclic voltammetry results in the potential window of 0.5–0.6 V (versus RHE). The chronoamperometric measurements were carried out at various potentials with a fixed time of 20 min. The gas-phase composition was analysed on a ThermoFisher Trace 1300 gas chromatography equipped with pulsed discharge and flame ionization detectors. High-purity helium (99.9999%) and nitrogen (99.9999%) were employed as carriers or make-up gases for the chromatography. A Bruker AVANCE-III HD 500 was utilized to detect the amounts of liquid products of electrolysis.

The FE for the gas products was calculated using the following equation:

$$FE = \frac{Q_{CO}}{Q_{total}} = \frac{Z \times n \times F}{Q_{total}}$$

where Q is the total charge collected through the applied working electrode, Z is the number of transfer electrons, which is 2 for both CO and H₂, n is the number of moles for a given product and F is the Faradaic constant with a value of 96,485 C mol⁻¹.

The TOF for CO formation was calculated as follows:

$$\text{TOF} = \frac{I_{\text{product}}/nF}{m_{\text{cat}}\omega/M_{\text{Ni}}}$$

where I_{product} is the partial current for a specific product, m_{cat} is the catalyst mass, ω is the Ni content of the catalyst and M_{Ni} represents the atomic mass of Ni (58.6934 g mol⁻¹). The cathodic energy efficiency of CO formation was calculated as follows³⁷:

$$\Phi_{\text{CO}} = \frac{\text{FE}(\%) \times \Delta E_{\text{CO}}^0}{\Delta E_{\text{CO}}}$$

where Φ_{CO} is the cathodic energy efficiency of CO formation, ΔE_{CO}^0 is the difference between the half-reaction potential for water oxidation (1.23 V versus RHE) and the potential for CO₂ reduction to CO (0.11 V versus RHE) and ΔE_{CO} is the difference between the half-reaction potential for water oxidation and the applied potential at the cathode.

Calculation of the surface molar concentration of Ni centres. The surface molar concentration for the electrochemical reactive Ni centres (Γ_0) was calculated according to the slope of the linear correlation between the appropriate peak current for the Ni³⁺/Ni²⁺ reduction curve and the varying scan rate³⁸:

$$\text{Slope} = \frac{n^2 F^2 A \Gamma_0}{4RT}$$

where n is 1, F represents the Faraday constant of 96,485 C mol⁻¹, A is the geometric surface area of the glassy carbon electrode (0.19625 cm²), Γ_0 is the surface reactive concentration (mol cm⁻²), R is the ideal gas constant of 8.314 J mol⁻¹ K⁻¹ and T is the temperature (room temperature of 298 K here).

In situ ESTEM measurement. The in situ ESTEM measurements were performed on a Hitachi HF5000 aberration-corrected scanning transmission environmental electron microscope equipped with a Hitachi heating rod, which can be heated from room temperature to 1,000 °C. The accelerating voltage was fixed at 200 kV. The in situ ESTEM measurements were made to record the dynamic process of the transformation of Ni species by pyrolyzing the mixture of dicyandiamide and carbon carrier adsorbed on the Ni-citrate complex. The programmed temperature heating system was raised from room temperature to 100 °C, 200 °C, 300 °C, 400 °C, 500 °C, 700 °C and 800 °C at a rate of 5 °C s⁻¹. Characterization of samples began 0.5 h after reaching a predetermined temperature.

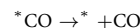
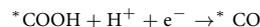
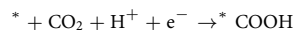
XAFS measurements. The ex situ X-ray absorption related data were gathered from beamline BL01C1 at the National Synchrotron Radiation Research Center (NSRRC), Taiwan, with technical supports from the Ceshigo Research Service (www.ceshigo.com), wherein the monochromator used was a Si(111) double crystal. The in situ XAFS measurements were carried out at the X-ray absorption spectroscopy beamline of the Australian Synchrotron (ANSTO) in fluorescence mode, with technical support from Ceshigo Research Service. Athena software was used to process the data for XANES and EXAFS.

In situ ATR-IR measurement. The in situ ATR-IR monitoring process was carried out using a Nicolet 6700 FTIR spectrometer armed with an MCT detector and a PIKE VeeMAX III ATR accessory. A single cell with 25 ml of 0.1 M KHCO₃ electrolyte was used as the reactor. The working electrode was monocrystalline silicon with a Au film substrate. Ag/AgCl was used as the reference electrode, while a Pt wire was used as the counter electrode. Before starting the tests, the device was purged with ultrapure water and the electrolyte was treated for 30 min with a continuous Ar flow to eliminate the possible influence of air. Then, CO₂ was introduced into the electrolyte for 30 min to achieve CO₂ saturation. The background spectrum was collected with no potential applied, and spectra were recorded during the electrolysis procedure under different potentials. A 4 cm⁻¹ resolution and 32 scans were applied in the collection of all the spectra. Potentials were corrected with respect to a reversible hydrogen electrode²⁸.

XANES theoretical simulation. The metal K edge XANES simulation was performed using JFEFF v.9.6.4 on the basis of density functional theory (DFT)-optimized structures. XANES simulation was conducted with full multiple scattering cut-off radius of 6 Å, self-consistent field cut-off radius of 5 Å and RPA-screened core hole. The Hedin-Lundqvist model was adopted in the energy-dependent exchange correlation potential. The theoretical XANES spectra of each metal as absorbing atoms in bimetallic centres were calculated and the two as-obtained XANES spectra were merged according to their equal weights³⁹.

Computational details. All calculations in this work were carried out using the Vienna Ab initio Simulation Package (VASP)⁴⁰, and the generalized gradient approximation⁴¹ of Perdew-Burke-Ernzerhof (PBE)⁴² functional with the projector augmented wave (PAW) method was considered in the whole DFT calculation. The energy cut-off for the plane-wave basis was set to 400 eV, the force on each atom and the self-consistent calculations were set for convergence of relaxation at less than 0.03 eV Å⁻¹ and 10⁻⁵ eV, respectively. The Brillouin zone integration was performed using 3 × 3 × 1 space and the van der Waals interaction of species and substrates used the PBE-D3 method.

The CO₂RR process was modelled as followed:



where the asterisk (*) means the surface catalytic sites.

The free energies of each step (CO₂RR) were calculated according to the following equation⁴⁰:

$$\Delta G = \Delta E_{\text{DFT}} + \Delta E_{\text{ZPE}} - T\Delta S$$

Constrained AIMD was used to estimate the kinetic barriers of CO₂ reduction to CO in a water environment. The solvation effects were taken into consideration in the calculated process using an explicit solvent model as CO₂RR involved in the proton and electron transfer. The cut-off energy of AIMD was set at 300 eV and the time step in the molecular dynamics was set to be 0.5 fs (refs. 43,44). The Helmholtz free energy was obtained from the 'slow growth' method, in which the initial state and final state can be calculated by thermodynamic integration⁴⁵:

$$W_{\text{IS} \rightarrow \text{FS}} = \int_{\zeta(\text{IS})}^{\zeta(\text{FS})} \left(\frac{\partial F}{\partial \zeta} \right) d\zeta$$

wherein ζ is a velocity of transformation, the work $W_{\text{IS} \rightarrow \text{FS}}$ corresponds to the free energy difference between the final and initial states, $\frac{\partial F}{\partial \zeta}$ is related to constrained molecular dynamics through the SHAKE algorithm. The value of ∂ was set to 0.0005 Å for the 'slow growth', along with the reaction coordinate⁴⁶.

All AIMD simulations employed only the gamma point with no symmetry and the NVT thermostat (300 K) was used to calculate free energy⁴⁷.

Data availability

Data supporting the findings of this study are available in the article and Supplementary Information. Source data are provided with this paper.

Received: 10 April 2022; Accepted: 11 July 2022;

Published online: 18 August 2022

References

- Sullivan, I. et al. Coupling electrochemical CO₂ conversion with CO₂ capture. *Nat. Catal.* **4**, 952–958 (2021).
- Digdaya, I. A. et al. A direct coupled electrochemical system for capture and conversion of CO₂ from oceanwater. *Nat. Commun.* **11**, 4412 (2020).
- Jin, S., Hao, Z., Zhang, K., Yan, Z. & Chen, J. Advances and challenges for the electrochemical reduction of CO₂ to CO: from fundamentals to industrialization. *Angew. Chem. Int. Ed. Engl.* **60**, 20627–20648 (2021).
- Gu, J., Hsu, C.-S., Bai, L., Chen, H. M. & Hu, X. Atomically dispersed Fe³⁺ sites catalyze efficient CO₂ electroreduction to CO. *Science* **364**, 1091–1094 (2019).
- Zhong, H. et al. Synergistic electroreduction of carbon dioxide to carbon monoxide on bimetallic layered conjugated metal-organic frameworks. *Nat. Commun.* **11**, 1409 (2020).
- Mitchell, S. & Pérez-Ramírez, J. Single atom catalysis: a decade of stunning progress and the promise for a bright future. *Nat. Commun.* **11**, 4302 (2020).
- Lin, L. et al. Synergistic catalysis over iron-nitrogen sites anchored with cobalt phthalocyanine for efficient CO₂ electroreduction. *Adv. Mater.* **31**, 1903470 (2019).
- Jouny, M., Luc, W. & Jiao, F. General techno-economic analysis of CO₂ electrolysis systems. *Ind. Eng. Chem. Res.* **57**, 2165–2177 (2018).
- Jiao, J. et al. Copper atom-pair catalyst anchored on alloy nanowires for selective and efficient electrochemical reduction of CO₂. *Nat. Chem.* **11**, 222–228 (2019).
- Ding, T. et al. Atomically precise dinuclear site active toward electrocatalytic CO₂ reduction. *J. Am. Chem. Soc.* **143**, 11317–11324 (2021).
- Li, Y. et al. Synergistic effect of atomically dispersed Ni-Zn pair sites for enhanced CO₂ electroreduction. *Adv. Mater.* **33**, 2102212 (2021).

12. Okamura, M. et al. A pentanuclear iron catalyst designed for water oxidation. *Nature* **530**, 465–468 (2016).
13. Rong, H., Ji, S., Zhang, J., Wang, D. & Li, Y. Synthetic strategies of supported atomic clusters for heterogeneous catalysis. *Nat. Commun.* **11**, 5884 (2020).
14. Yang, Y. et al. O-coordinated W-Mo dual-atom catalyst for pH-universal electrocatalytic hydrogen evolution. *Sci. Adv.* **6**, eaba6586 (2020).
15. Qi, K. et al. Single-atom cobalt alloy bound to distorted 1T MoS₂ with ensemble effect for hydrogen evolution catalysis. *Nat. Commun.* **10**, 5231 (2019).
16. Wei, S. et al. Direct observation of noble metal nanoparticles transforming to thermally stable single atoms. *Nat. Nanotechnol.* **13**, 856–861 (2018).
17. Qiao, B. et al. Single-atom catalysis of CO oxidation using Pt₁/FeO_x. *Nat. Chem.* **3**, 634–641 (2011).
18. Yang, H. B. et al. Atomically dispersed Ni(I) as the active site for electrochemical CO₂ reduction. *Nat. Energy* **3**, 140–147 (2018).
19. Li, J. et al. A general strategy for preparing pyrrolic-N₄ type single-atom catalysts via pre-located isolated atoms. *Nat. Commun.* **12**, 6806 (2021).
20. Chen, B. et al. Enhancement of mass transfer for facilitating industrial-level CO₂ electroreduction on atomic Ni–N₄ sites. *Adv. Energy Mater.* **11**, 2102152 (2021).
21. Jouny, M., Luc, W. & Jiao, F. High-rate electroreduction of carbon monoxide to multi-carbon products. *Nat. Catal.* **1**, 748–755 (2018).
22. Shi, R. et al. Efficient wettability-controlled electroreduction of CO₂ to CO at Au/C interfaces. *Nat. Commun.* **11**, 3028 (2020).
23. Dinh, C.-T. et al. CO₂ electroreduction to ethylene via hydroxide-mediated copper catalysis at an abrupt interface. *Science* **360**, 783–787 (2018).
24. Ni, W. et al. Electroreduction of carbon dioxide driven by the intrinsic defects in the carbon plane of a single Fe–N₄ Site. *Adv. Mater.* **33**, 2003238 (2021).
25. Wang, J., Zhong, H.-x., Wang, Z.-l., Meng, F.-l. & Zhang, X.-b. Integrated three-dimensional carbon paper/carbon tubes/cobalt-sulfide sheets as an efficient electrode for overall water splitting. *ACS Nano* **10**, 2342–2348 (2016).
26. Diercks, C. S., Liu, Y., Cordova, K. E. & Yaghi, O. M. The role of reticular chemistry in the design of CO₂ reduction catalysts. *Nat. Mater.* **17**, 301–307 (2018).
27. Firet, N. J. & Smith, W. A. Probing the reaction mechanism of CO₂ electroreduction over Ag films via operando infrared spectroscopy. *ACS Catal.* **7**, 606–612 (2017).
28. Zhu, W. et al. Enhanced CO₂ electroreduction on neighboring Zn/Co monomers by electronic effect. *Angew. Chem. Int. Ed. Engl.* **59**, 12664–12668 (2020).
29. Zhang, X. et al. Molecular engineering of dispersed nickel phthalocyanines on carbon nanotubes for selective CO₂ reduction. *Nat. Energy* **5**, 684–692 (2020).
30. Li, Z. et al. Iridium single-atom catalyst on nitrogen-doped carbon for formic acid oxidation synthesized using a general host–guest strategy. *Nat. Chem.* **12**, 764–772 (2020).
31. Wan, X. et al. Fe–N–C electrocatalyst with dense active sites and efficient mass transport for high-performance proton exchange membrane fuel cells. *Nat. Catal.* **2**, 259–268 (2019).
32. Zhao, X. & Liu, Y. Unveiling the active structure of single nickel atom catalysis: critical roles of charge capacity and hydrogen bonding. *J. Am. Chem. Soc.* **142**, 5773–5777 (2020).
33. Zhao, X. & Liu, Y. Origin of selective production of hydrogen peroxide by electrochemical oxygen reduction. *J. Am. Chem. Soc.* **143**, 9423–9428 (2021).
34. Chen, J.-W. et al. Pseudo-adsorption and long-range redox coupling during oxygen reduction reaction on single atom electrocatalyst. *Nat. Commun.* **13**, 1734 (2022).
35. Pan, Y., Zhang, C., Liu, Z., Chen, C. & Li, Y. Structural regulation with atomic-level precision: from single-atomic site to diatomic and atomic interface catalysis. *Matter* **2**, 78–110 (2020).
36. Zhang, L. et al. Atomic layer deposited Pt–Ru dual-metal dimers and identifying their active sites for hydrogen evolution reaction. *Nat. Commun.* **10**, 4936 (2019).
37. Kumar, B. et al. Reduced SnO₂ porous nanowires with a high density of grain boundaries as catalysts for efficient electrochemical CO₂-into-HCOOH conversion. *Angew. Chem. Int. Ed. Engl.* **56**, 3645–3649 (2017).
38. Pintado, S., Goberna-Ferrón, S., Escudero-Adán, E. C. & Galán-Mascarós, J. R. Fast and persistent electrocatalytic water oxidation by Co-Fe Prussian Blue coordination polymers. *J. Am. Chem. Soc.* **135**, 13270–13273 (2013).
39. Wang, Y. et al. Coordination number regulation of molybdenum single-atom nanozyme peroxidase-like specificity. *Chem* **7**, 436–449 (2021).
40. Kresse, G. & Furthmüller, J. Efficiency of ab-initio total energy calculations for metals and semiconductors using a plane-wave basis set. *Comp. Mater. Sci.* **6**, 15–50 (1996).
41. Blöchl, P. E. Projector augmented-wave method. *Phys. Rev. B* **50**, 17953–17979 (1994).
42. Perdew, J. P. et al. Atoms, molecules, solids, and surfaces: applications of the generalized gradient approximation for exchange and correlation. *Phys. Rev. B* **46**, 6671–6687 (1992).
43. Kresse, G. & Hafner, J. *Ab initio* molecular dynamics for liquid metals. *Phys. Rev. B* **47**, 558–561 (1993).
44. Grimme, S., Antony, J., Ehrlich, S. & Krieg, H. A consistent and accurate *ab initio* parametrization of density functional dispersion correction (DFT-D) for the 94 elements H–Pu. *J. Chem. Phys.* **132**, 154104 (2010).
45. Wellendorff, J. et al. Density functionals for surface science: exchange-correlation model development with Bayesian error estimation. *Phys. Rev. B* **85**, 235149 (2012).
46. Mathew, K., Sundararaman, R., Letchworth-Weaver, K., Arias, T. & Hennig, R. G. Implicit solvation model for density-functional study of nanocrystal surfaces and reaction pathways. *J. Chem. Phys.* **140**, 084106 (2014).
47. Mathew, K., Kolluru, V. S. C., Mula, S., Steinmann, S. N. & Hennig, R. G. Implicit self-consistent electrolyte model in plane-wave density-functional theory. *J. Chem. Phys.* **151**, 234101 (2019).

Acknowledgements

H.X.Z. acknowledges funding from the Alexander von Humboldt Foundation. This work was supported by the National Natural Science Foundation of China (21725103, 51925102), National Key R&D Program of China (2020YFB1505603, 2019YFA0705704), Jilin Province Science and Technology Development Plan Funding Project (20200201079J) and Youth Innovation Promotion Association CAS (2021223).

Author contributions

X.B.Z. conceived and designed the project. Q.H. synthesized the materials. Q.H. and K.H.L. carried out the electrochemical testing. H.X.Z., Q.H., K.H.L. and D.X.L. contributed to the characterization and related discussion. Q.H. and N.Z. performed in situ ATR-IR measurements. J.Z.W. contributed to the theoretical calculations. Z.H.R., X.L. and L.W.C. contributed to the in situ ESTEM measurements. X.Z. contributed to the XANES simulations. H.Z. and J.L. contributed to the STEM simulation. Q.H., H.X.Z., K.H.L., J.Z.W., J.M.Y. and X.B.Z. co-wrote the paper. All the authors discussed the results and commented on the manuscript.

Competing interests

The authors declare no competing interests.

Additional information

Supplementary information The online version contains supplementary material available at <https://doi.org/10.1038/s44160-022-00138-w>.

Correspondence and requests for materials should be addressed to Xin-bo Zhang.

Peer review information *Nature Synthesis* thanks Shaojun Guo and the other, anonymous, reviewer(s) for their contribution to the peer review of this work. Primary Handling Editor: Alexandra Groves, in collaboration with the *Nature Synthesis* team.

Reprints and permissions information is available at www.nature.com/reprints.

Publisher's note Springer Nature remains neutral with regard to jurisdictional claims in published maps and institutional affiliations.

Springer Nature or its licensor holds exclusive rights to this article under a publishing agreement with the author(s) or other rightsholder(s); author self-archiving of the accepted manuscript version of this article is solely governed by the terms of such publishing agreement and applicable law.

© The Author(s), under exclusive licence to Springer Nature Limited 2022